scientific reports

Check for updates

OPEN

Heptamethine cyanine-based polymeric nanoparticles for photothermal therapy in HCT116 human colon cancer model

Sastiya Kampaengsri[1,6], Gong Yi Yong[2,6], Sirimongkon Aryamueang[1], Bongkot Ouengwanarat[1], Thitima Pewklang[1], Kantapat Chansaenpak[3], Sarawut Jitrapakdee[4], Chin-Siang Kue[5]✉ & Anyanee Kamkaew[1]✉

In this work, we synthesize a quinoline-based heptamethine cyanine, QuCy7, with sulfonate groups to enhance water solubility. This dye demonstrates exceptional near-infrared absorption beyond 750 nm, accompanied by photothermal properties but low photostability. Encapsulating QyCy7 with polyethylene glycol to form nanopolymer, QuCy7@mPEG NPs, addresses the issue of its photoinstability. TEM showed that QuCy7@mPEG NPs possess a spherical morphology, featuring a core-shell structure with a size of around 120 nm in diameter. Upon irradiation with an 808 nm laser for 10 min, a significant increase in temperature up to 24 °C can be achieved with a photothermal conversion (PTC) rate of approximately 35%. QuCy7@mPEG NPs exhibit remarkable photothermal stability as compared to QuCy7. The efficiency of QuCy7@mPEG NPs was demonstrated by the *in vitro* PTT studies. Finally, the nanoparticles' acute toxicity and effectiveness were assessed using the chick embryo model. The results provide compelling evidence that QuCy7@mPEG NPs are safe without inducing hemolysis, inhibit angiogenesis when exposed to light, and exhibit anti-tumor activity with a 76% reduction in tumor size compared to QuCy7 (40%). Thus suggesting the sulfonate groups can enhance water solubility, and its nanopolymer is biocompatible and possesses superior anti-tumor efficacy.

Keywords NIR photosensitizer, PTT, cancer therapy, nanomedicine, heptamethine cyanine, chick embryo

Photothermal therapy (PTT) is a modern approach to cancer treatment that offers non- or minimally invasive procedures. It involves utilizing a photosensitizer to absorb light in the near-infrared (NIR) region, converting it into heat, and inducing apoptosis in targeted cells[1]. In recent years, nanoscale materials incorporating PTT have gained much interest. These nanoparticles, which range in size from 20 to 300 nm, preferentially accumulate in tumor tissues due to the enhanced permeability and retention (EPR) effect[2]. As a result, most researchers used nanoparticles as a drug or chemical, including PTT agents, to treat cancer[3].

Gold nanorods[4], gold nanosheets, sulfide nanoparticles[5], and metal/metal oxide nanoparticles[6–8] have all been investigated as potential PTT photosensitizers. Despite their excellent light absorption, photothermal conversion, and photostability properties, these materials pose challenges due to their lack of biodegradability and potential long-term toxicity in medical applications[9–12]. Organic-based nanoparticles featuring organic small-molecule photosensitizers offer a more promising alternative[13]. Compounds such as aza-boron-dipyrromethene[14,15], porphyrins[16,17], diketopyrrolopyrroles[18], croconaines[19,20], squaraines[21], and cyanines[22] exhibit desirable biocompatibility and degradability once they form nanoparticles. These organic-based nanoparticles represent a better-suited option for safe and effective PTT in medical practice.

[1]School of Chemistry, Institute of Science, Suranaree University of Technology, Nakhon Ratchasima 30000, Thailand. [2]School of Graduate Studies, Management and Science University, Seksyen 13, Shah Alam 40100, Selangor, Malaysia. [3]National Nanotechnology Center, National Science and Technology Development Agency, Thailand Science Park, Pathum Thani 12120, Thailand. [4]Department of Biochemistry, Faculty of Science, Mahidol University, Bangkok, Thailand. [5]Faculty of Health and Life Sciences, Management and Science University, Seksyen 13, 40100 Shah Alam, Selangor, Malaysia. [6]Sastiya Kampaengsri and Gong Yi Yong contributed equally to this work. ✉email: cskue@msu.edu.my; anyanee@sut.ac.th

A NIR-absorbing dye, indocyanine green (ICG), has been loaded into PEG-modified black phosphorus nanosheets (ICG@BPNS-PEG) to create the real-time fluorescence-guided tumor location with PTT for breast cancer therapy[23]. The PTT ability and photostability of the nanoparticles ICG@BPNS-PEG were much better than those of the free ICG dye, with a temperature increase of 18.21 °C, while the free ICG dye only increased by 12.99 °C. Furthermore, these nanoparticles demonstrate superior passive tumor-targeting accumulation via the EPR effect[23]. These findings revealed that the incorporation of organic small-molecule photosensitizers into nanoparticles enhances photostability and PTT efficacy. Additionally, because of the properties of the nanoparticles, biocompatibility is also enhanced.

Heptamethine cyanine dyes (Cy7) are another well-known fluorescent dye with a structure similar to ICG that is highly capable of both absorption and emission of light in the NIR spectrum. In addition, they are widely used as photosensitizers in various biological applications[24]. Numerous studies have shown that these cyanine dyes perform well in both photothermal therapy (PTT) and photodynamic therapy (PDT), indicating promising in vivo activities[24]. However, their use in biosystems is limited due to their low aqueous solubility and photostability, which reduces their overall efficiency[25]. Thus, the incorporation of these dyes within nanoparticles is important[26].

Figure 1 shows the typical structures of Cy7, which consist of two indole rings linked to a methine chain. Numerous attempts have been made to alter various components of Cy7's structure (positions $(CH_2)_n$, X, Y, R_1, and R_2) to increase its effectiveness or incorporate it into different types of nanoparticles[27,28]. However, there has been little research into replacing indole rings with alternative heterocyclic aromatic rings such as quinoline rings, especially in biological research[29].

In this work, we first attempted substituting the indolium ring with *N*-ethylated quinolinium rings. Surprisingly, this alteration produced a cyanine dye-based quinoline with superior photothermal characteristics, i.e. higher heat conversion. Unfortunately, the dye displayed photo instability upon irradiation. To overcome this limitation, we extend the aliphatic chain as a vibrational unit[30] at the N position of quinolinium, leaving the sulfate group at the end of the chain to promote water solubility (QuCy7, Fig. 1). Subsequently, the dye was encapsulated with methoxy polyethylene glycol (mPEG) to improve its stability and biocompatibility. Following that, the photophysical and thermal properties, dye stability, and biological applications of these nanoparticles—quinoline-based cyanine dye nanoparticles, or QuCy7@mPEG NPs—were investigated.

Results and discussions

Synthesis of QuCy7

Quinoline-based cyanine (QuCy7) was synthesized using an approach akin to that of the most widely used Cy7 (Fig. 2A). This involved the assembly of two distinct components, namely bis-carbaldehyde and two equivalents of *N*-heterocyclic aromatic ring, under basic conditions. The synthesis of the bis-carbaldehyde precursor, Compound I, began with preparingVilsmeier's reagent, which involved the reaction of oxalyl chloride with dimethylformamide. The reagent was then treated with cyclohexanone and refluxed for a few hours. After that, the mixture was hydrolyzed with iced water to yield the product. Another part of QuCy7 is quinolinium salt, Compound II, which was prepared through the nucleophilic substitution reaction between 2-methyl quinoline and 1,4-butane sultone. The reaction was carried out under microwave radiation. Finally, QuCy7 was synthesized by condensing Compound I and two equivalents of Compound II using Knoevenagel condensation with piperidine as a base. The product's structure was confirmed using NMR and ESI mass spectroscopy (Figure S1).

Preparation, characterizations, and optical properties of QuCy7@mPEG NPs

Subsequently, QuCy7@mPEG NPs were formed by encapsulating QuCy7 free dye and mPEG at a ratio of 1:1 (Fig. 2B). By using MALDI-TOF mass spectrometry, the nanoparticle's mass after encapsulation was found to be 5328 g/mol (Figure S2), indicating that the mass of QuCy7 (694.28 g/mol) is combined with a mass of m-PEG (5000 g/mol). Furthermore, QuCy7@mPEG NPs revealed a NIR absorption profile similar to QuCy7, implying the PEGylation did not alter the optical property of the dye[31,32] (Fig. 3A). In addition, after irradiation, the heat-generating ability of the NPs does not significantly change, indicating that QuCy7@mPEG has excellent

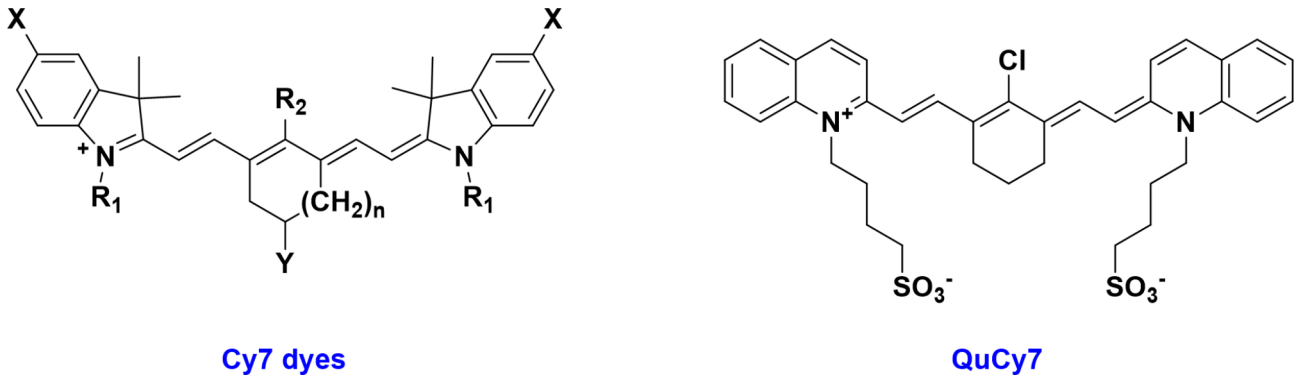

Fig. 1. Typical structures of heptamethine cyanine dyes (Cy7) and structure of the dye in this work (QuCy7).

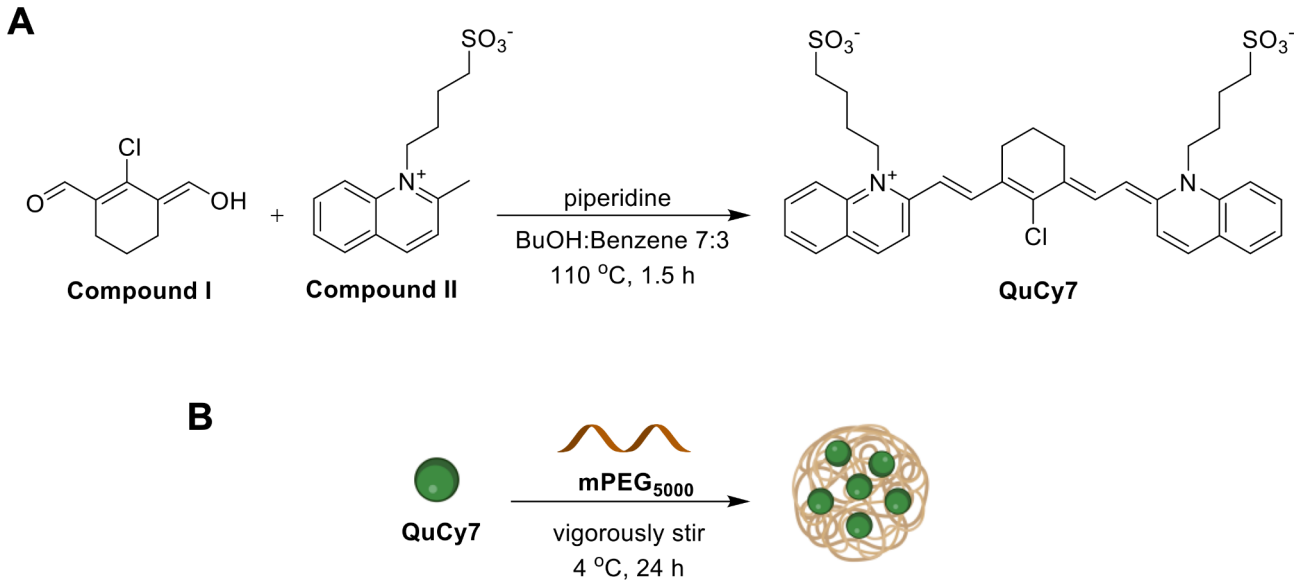

Fig. 2. (**A**) Synthesis of QuCy7 and (**B**) preparation of QuCy7@mPEG NPs.

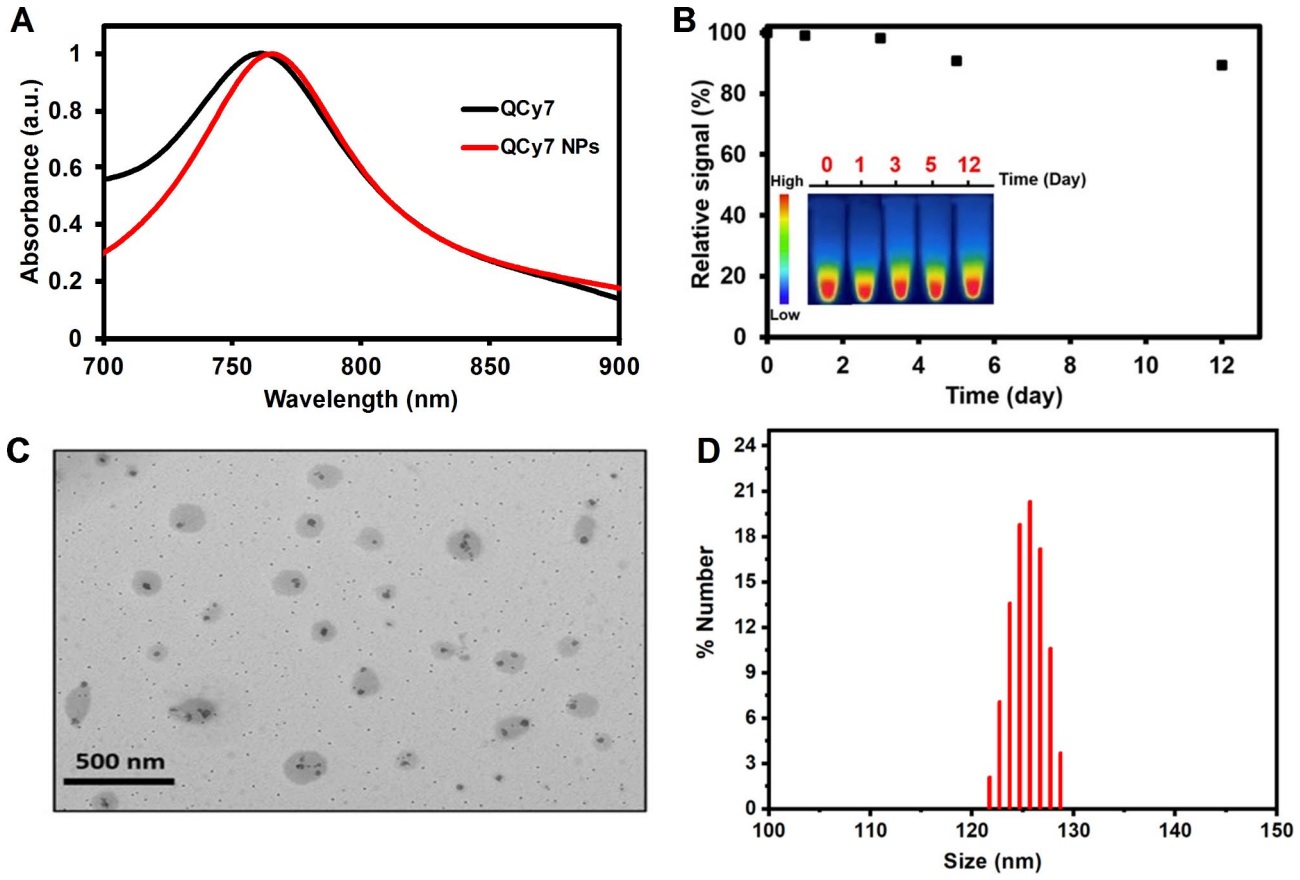

Fig. 3. (**A**) Absorption spectra of QuCy7 and QuCy7@mPEG NPs. (**B**) Heat stability of QuCy7@mPEG NPs over time. Inset: Photograph of heat stability of the QuCy7@mPEG NPs. (**C**) TEM image of QuCy7@mPEG NPs. (**D**) HD size distribution histogram of QuCy7@mPEG NPs in water measured by DLS.

photostability for at least 12 days. (Fig. 3B). Moreover, the absence of the fluorescence signal at different excitations raises the possibility of nonradiative vibrational relaxation (Figure S3)[33,34]. Furthermore, the concentration of QuCy7 in the nanoparticles was estimated using the absorbance calibration curve shown in Figure S4.

The spherical morphology of QuCy7@mPEG NPs with a diameter of about 120 nm is depicted in the transmission electron microscopy (TEM) image (Fig. 3C). The observation of the core–shell architecture further supports the incorporation of a soft lyophilic mPEG shell and a dense QuCy7 core. In addition, the dynamic light scattering (DLS) result shown in Fig. 3D suggests that the average size of QuCy7@mPEG NPs was 126 ± 8.2 nm, which agrees with the TEM result. This indicates that QuCy7@mPEG NPs are ideal for blood artery circulation due to the EPR effect[35–37]. The stability of the NPs was assessed by measuring their absorbances, zeta potentials, and particle sizes over seven days in DI water, PBS, DMEM-based cellular medium, and FBS (Figure S5 and Table S1). After three days, the average size profiles of all media dispersions are 52–54 nm (FBS), 254–291 nm (PBS), 267–274 nm (DMEM), and 126–167 nm (DI water), suggesting particle stability. Nevertheless, the NPs showed some instability in their agglomeration behavior at day 7, with typical agglomerate sizes rising by roughly 10 to 100 nm (Table S1). While QuCy7@mPEG NPs exhibit similar hydrodynamic sizes in DI, PBS, and DMEM, they are substantially smaller in FBS (Table S1). This might be due to the PBS-stabilized particle dispersion[38]. Interestingly, the zeta potential did not vary much over time in any of the tested media. However, the values are around ± 10 to ± 30 mV in DI and FBS, suggesting incipient stability, and ± 30 to ± 40 mV in PBS and DMEM, implying moderate stability[39,40] (Table S1).

Photothermal properties

To investigate the photothermal effect of QuCy7@mPEG NPs, the NP solutions at various concentrations of 250, 500, 750, and 1000 µg/ mL were irradiated using an 808 nm laser (1.0 W/ cm^2). As shown in Fig. 4A, the solution temperature progressively increased under photoirradiation, and the rate of temperature increase is connected with the concentration of QuCy7@mPEG NPs. The temperature of the solution quickly increased to about 15 °C after 2 minutes of exposure at a concentration of 1000 µg/mL, and temperature elevation (ΔT) climbed to 24 °C in 10 min, indicating the good photothermal activity of QuCy7@mPEG NPs. The NPs demonstrated a photothermal conversion efficiency (PCE) of 35.5 (Figure S6), comparable to sulfonate-containing hepthamethine cyanine dyes (Table S2). Furthermore, a slight change in the temperature of the NPs was observed at the fourth cycle (OFF – ON laser, Fig. 4B), indicating that QuCy7@mPEG NPs exhibit photothermal stability for a maximum of three radiation exposure cycles. On the other hand, the temperature of QuCy7 (free dye) increased to about

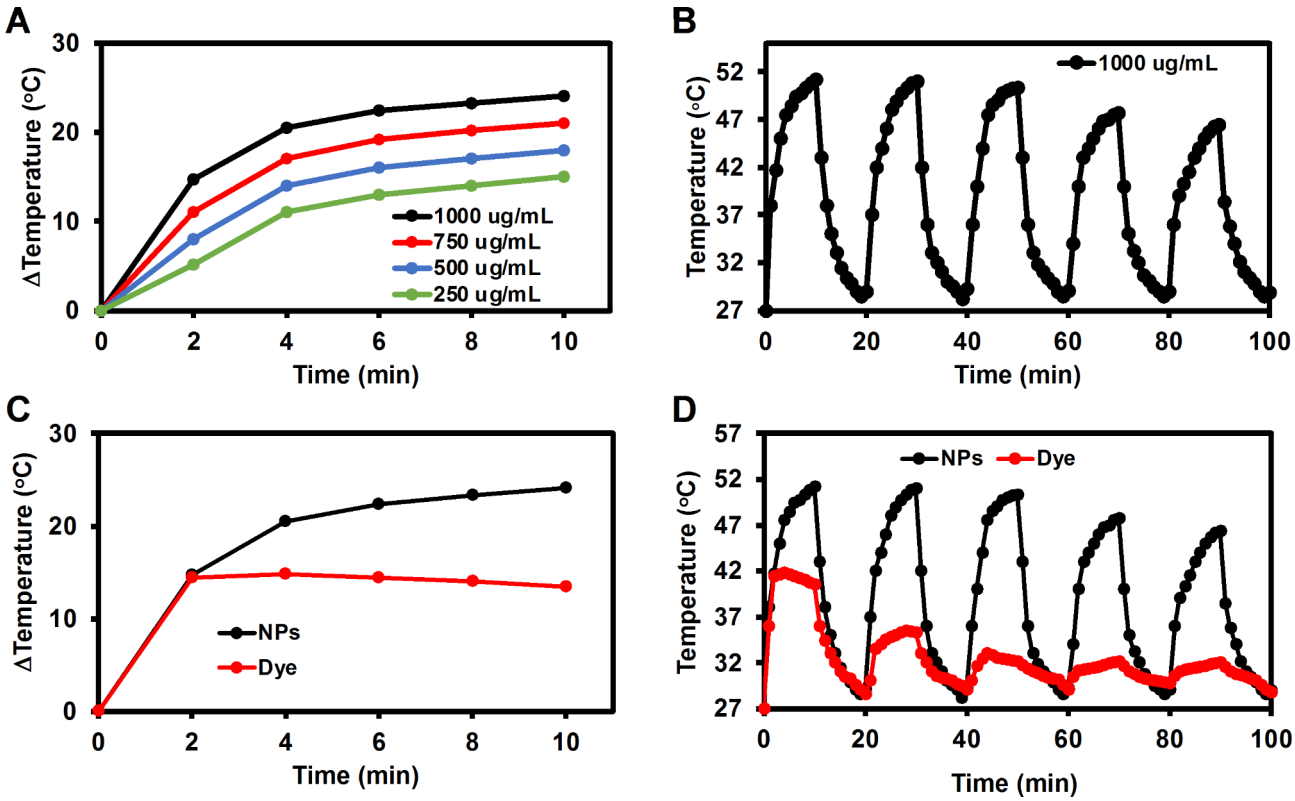

Fig. 4. (**A**) Heating curves of QuCy7@mPEG NPs at various concentrations after irradiation with an 808 nm laser at a power density of 1 W/cm^2. (**B**) Photothermal handling test of QuCy7@mPEG NPs (1000 µg/mL) during five alternate heating – cooling cycles. (**C**) Heating curves of QuCy7 and QuCy7@mPEG NPs in aqueous solution after irradiation with an 808 nm laser at a power density of 1 W/cm^2. (**D**) Photothermal handling test of QuCy7 and QuCy7@mPEG NPs during five alternate heating – cooling cycles.

14 °C after 60 s of radiation at the same concentration. Then, in less than ten minutes, it slightly decreased to 12 °C, suggesting that QuCy7's photothermal activity was less stable than that of QuCy7@mPEG NPs (Fig. 4C). There is a greater disparity between the OFF – ON laser cycles. Unlike QuCy7@mPEG NPs, the temperature of the solution containing free dye rose 60 s after irradiation and then rapidly dropped after the first cycle (Fig. 4D). These findings suggest that encapsulating the dye inside NPs could increase its photostability.

In vitro photothermal effect

A relative cell viability assay was performed to evaluate the phototoxicity of QuCy7@mPEG NPs on a human colorectal carcinoma (HCT116) cell line. In the absence of laser irradiation, the cell survival was over 90%, even at concentrations up to 3 mg/mL, indicating low dark cytotoxicity and excellent biocompatibility (Fig. 5A). However, under 808 nm photoirradiation for 5 min (1.0 W/ cm^2), the cell viability decreased as the concentration of QuCy7@mPEG NPs increased. The IC_{50} was calculated to be 0.7 mg/mL (Figure S7). Furthermore, using the live/dead cell assay, it was possible to evaluate the photocytotoxicity of the NPs both before and after laser irradiations. Living cells react with non-fluorescent calcein acetomethoxy (Calcein-AM) when it is administered, producing green fluorescence (excited at 488 nm) through a reaction with esterase. On the other hand, red fluorescence (λ_{ex} = 590 nm) can be produced by propidium iodide (PI) when it intercalates between

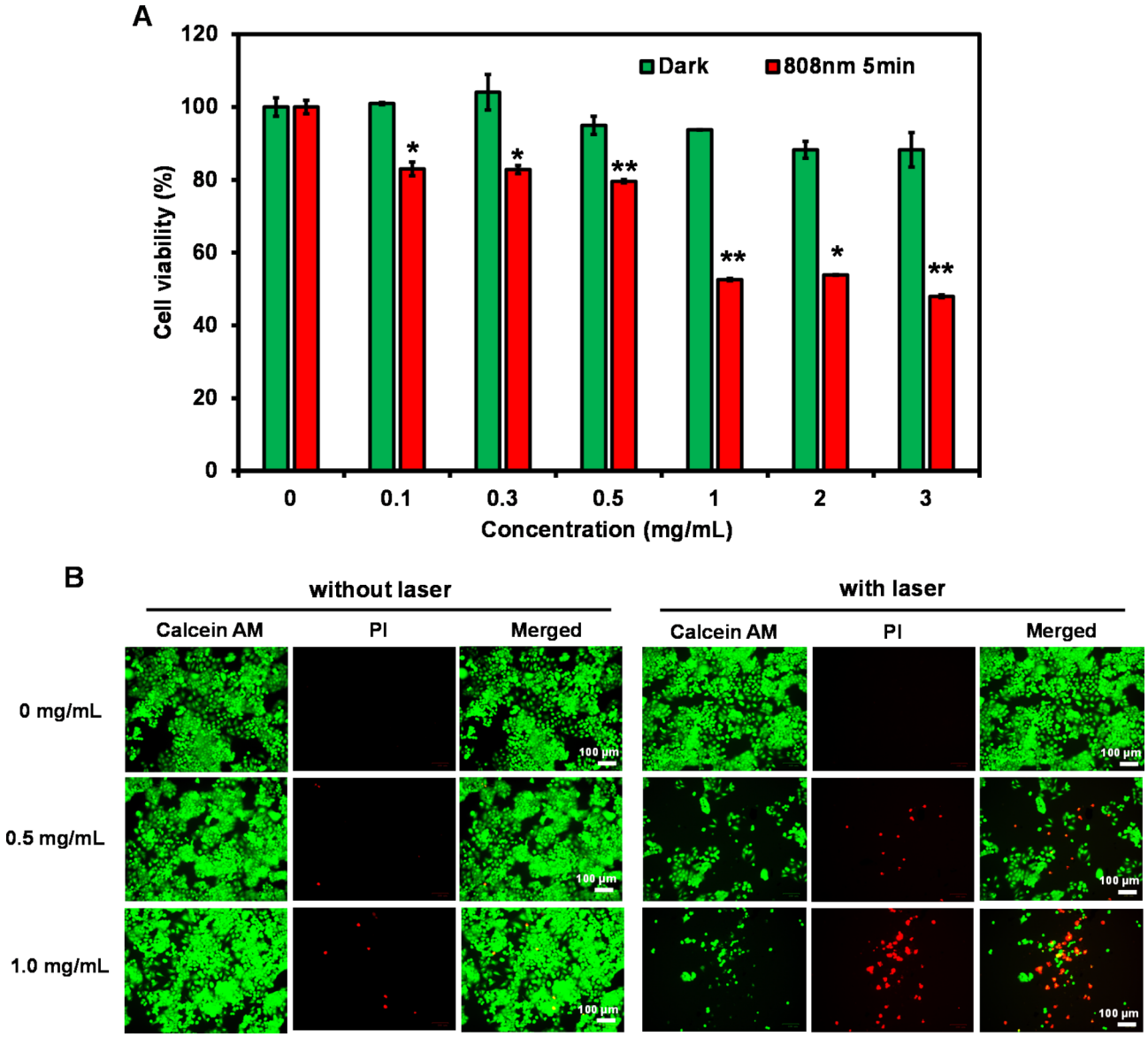

Fig. 5. (**A**) The relative cell viability of HCT116 cells performed by MTT assay under 808 nm photoirradiation for 5 min (1 W/cm^2) following incubation with QuCy7@mPEG NPs (0–3.0 mg/mL) for 24 h. Data are presented as means ± SD ($n = 3$), $^*p < 0.05$, or $^{**}p < 0.01$ based on Student's *t-test*. (**B**) Fluorescent images of LIVE/DEAD co-staining assays of HCT116 cells after treatment with QuCy7@mPEG NPs (0, 0.5, and 1.0 mg/mL) for 24 h before irradiating for 5 min.

complementary bases of DNA and enters the nucleus of dead cells through the membrane. As illustrated in Fig. 5B, the non-irradiated HCT116 cells produced negligible red fluorescence, while the HCT116 cells treated with QuCy7@mPEG NPs and then laser irradiated, displayed strong red fluorescence, particularly at a dose of 1 mg/mL, indicating a higher heat conversion was required to trigger cell death.

Hemocompatibility test and microscopical evaluation of QuCy7@mPEG NPs on chick embryo red blood cells

Hemocompatibility holds an important role in therapeutic approaches designed for intravenous administration. In this study, red blood cells (RBC) from the chick embryo were used as a model to investigate this effect. As shown in Fig. 6A&B, QuCy7@mPEG NPs did not induce hemolysis on the RBC as the supernatant remained macroscopically clear at all tested concentrations (15 mg/mL-60 mg/mL). In contrast, distilled water induced total hemolysis, producing a reddish supernatant, indicating the release of hemoglobin from the ruptured red blood cells. Upon Hematoxylin and Eosin (H&E)-stained blood smear light microscopic observation, QuCy7@mPEG NPs-treated blood displayed the intact oval-shaped nucleated chick RBC comparable to the PBS-treated negative control. However, the distilled water-treated RBC showed destruction of the RBC membranes (Fig. 6C).

In ovo acute toxicity and PTT-induced anti-angiogenesis

The chick embryo model has emerged as a preliminary test for the toxicity and efficacy of novel nanoparticles, enabling the rapid screening of the pharmacological and therapeutic behavior of the nanoparticles under relevant physiological conditions and providing more ethical means of qualifying the nanoparticle for *in vivo* testing[41,42]. The acute toxicity of QuCy7@mPEG NPs was determined at 48-hour post-administration into chick embryos. In this study, the LC_{50} value of the QuCy7@mPEG NPs was not determined as the tested concentrations up to 15 mg/mL (equivalent to mg/kg) were not lethal to the chick embryo. This suggests the great biocompatibility and well-tolerability of QuCy7@mPEG NPs, hence, 15 mg/mL of QuCy7@mPEG NPs was selected for the evaluation of PTT-induced anti-angiogenesis and antitumor.

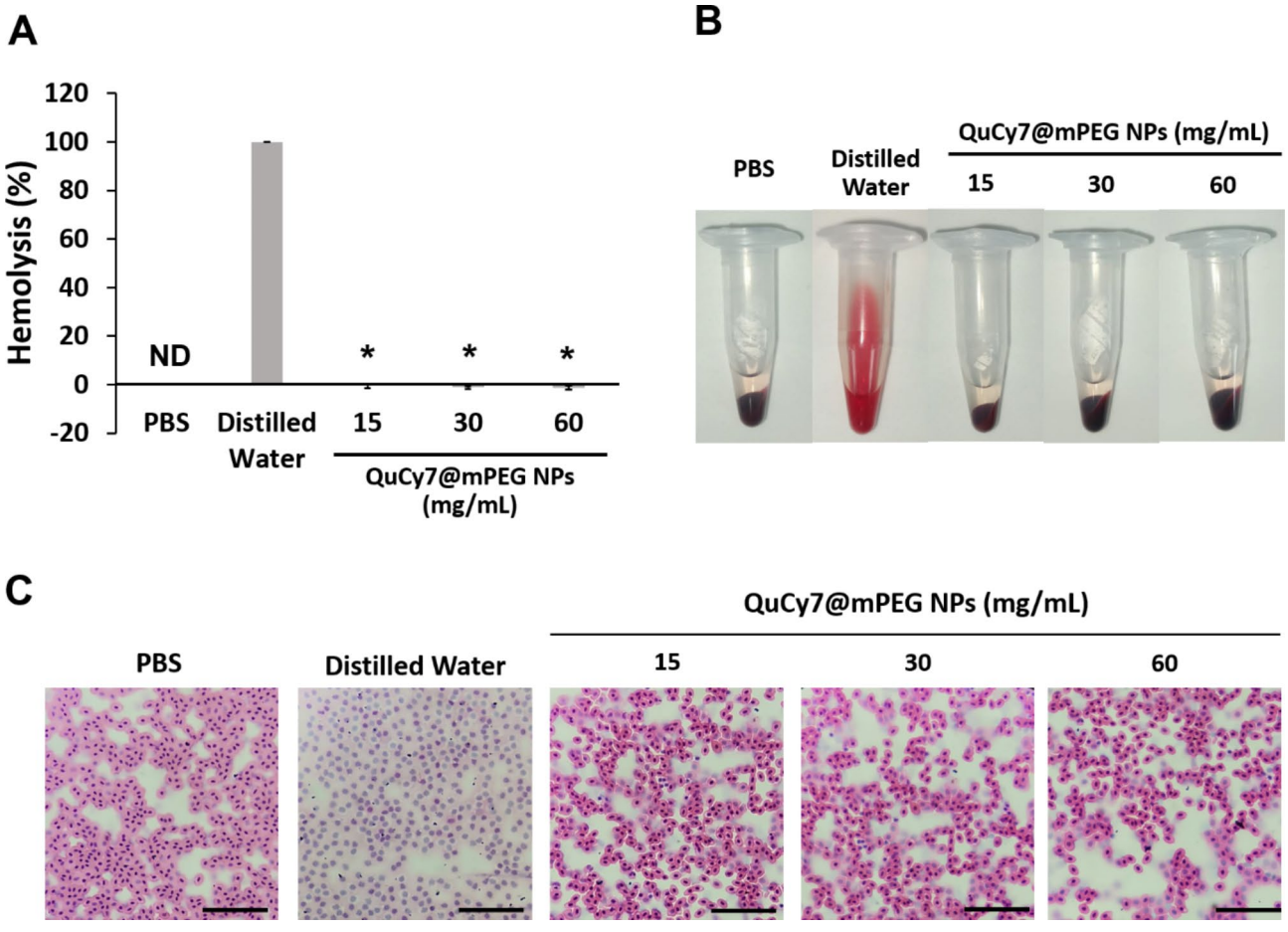

Fig. 6. (**A**) The hemolysis percentage of QuCy7@mPEG NPs. Data are presented as means ± SD ($n = 5$), $^{*}p < 0.0001$, positive control distilled water vs. QuCy7@mPEG NPs. (**B**) The macroscopic observation of RBC supernatant post-centrifugation at 1 h after incubation. (**C**) The representative H&E-stained blood smear of RBC post-hemolytic analysis (scale bar = 80 µm, magnification 400×).

The photothermal-induced anti-angiogenesis ability of QuCy7@mPEG NPs, mPEG, and QuCy7 were evaluated using the chorioallantoic membrane (CAM) model. The saline- and mPEG (13.2 mg/mL)-treated CAMs showed unchanged in the blood vessel structure post-PTT. In contrast, QuCy7@mPEG NPs (15 mg/mL) and QuCy7 (1.8 mg/mL; equivalent to the QuCy7 in QuCy7@mPEG NPs at 15 mg/mL) induced visible vascular destructions at 10 min post-PTT in the CAMs. The QuCy7-treated CAM showed the destruction of tiny vasculatures compared to pre-PTT, while QuCy7@mPEG NPs induced a large area of severe damage to the blood post-PTT (Fig. 7A). As shown in Fig. 7B, quantification of the vascular destruction revealed saline and mPEG-treated CAMs displayed no angio-destructive activity, while there is approximately 20% higher vasculature damage for QuCy7@mPEG NPs (61.48 ± 5.53%) than the QuCy7 (41.59 ± 4.61%)-treated CAMs ($p = 0.025$). The negative vascular destruction in saline and mPEG control might be due to vasodilation. These findings indicated that mPEG nanocarrier improves the PTT-mediated vasculature damage of QuCy7, similar to another study[43].

Additionally, histological analysis demonstrated that the membrane's H&E staining in CAMs after PTT demonstrated a typical blood vessel anatomical morphology. The blood vessel rupture was seen in the QuCy7@mPEG NPs and QuCy7-treated CAMs, along with the extravasation of nucleated chick erythrocytes (Fig. 7C). In addition, a significant reduction in the thickness of the CAMs accompanied by the destruction of the ectoderm in the QuCy7@mPEG NPs (0.09 ± 0.01 mm) and QuCy7 (0.18 ± 0.02 mm)-treated CAMs ($p < 0.001$) was observed (Fig. 6D), compared to saline and mPEG-treated group at 0.49 ± 0.06 mm and 0.47 ± 0.01 mm, respectively.

In ovo PTT anti-tumor study

The anti-tumor efficacy of QuCy7@mPEG NPs was evaluated *in ovo* using human HCT116-implanted tumor xenograft in CAMs. The real-time localized temperature of the tumor tissue was monitored and recorded throughout the photo-irradiation, after 15 min of intravenous administration. The temperature in the saline- and mPEG-treated tumor was maintained between 36 and 37 °C throughout photo-irradiation compared to pre-irradiation (Figure S8). Conversely, a gradual increase in temperature was observed in QuCy7 and QuCy7@mPEG NPs-treated tumor, reaching the peak at 100 s of photo-irradiation at 37 °C for QuCy7 and 41 °C for QuCy7@mPEG NPs-treated tumor, respectively (Fig. 8A). The observed 1 °C increase in QuCy7 might be due to its poor infiltration into the tumor tissue compared to QuCy7@mPEG NPs.

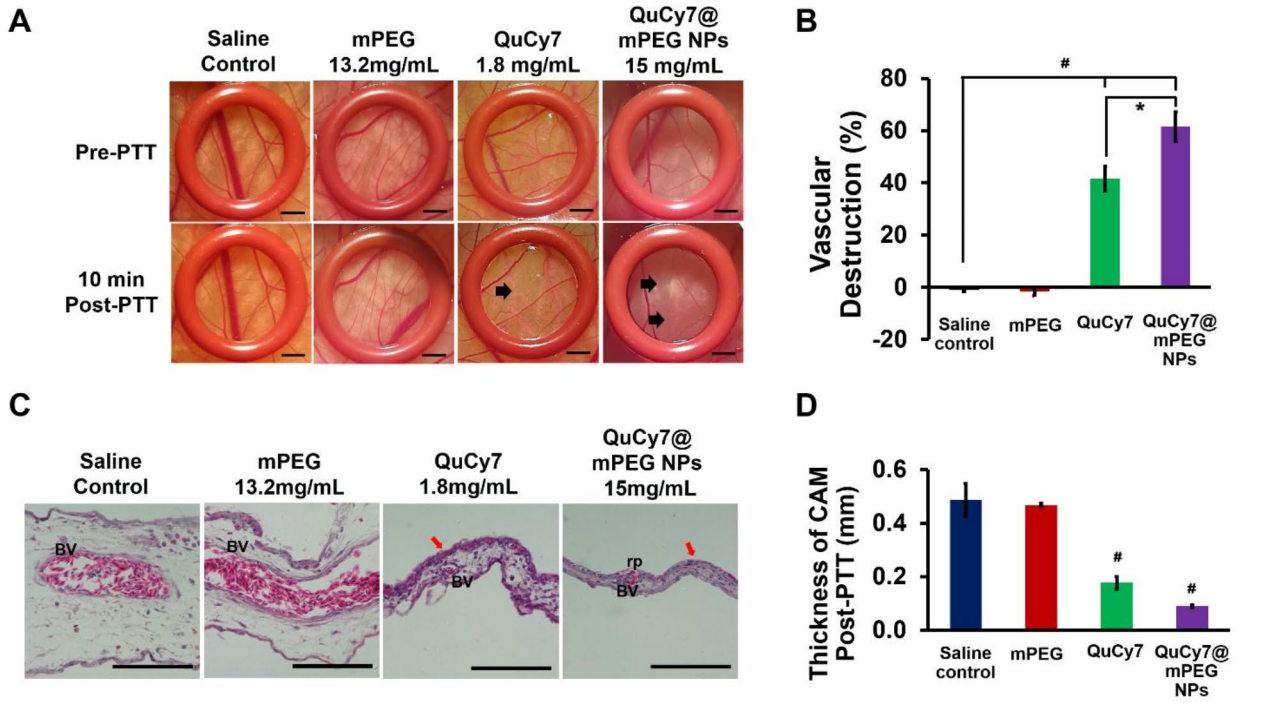

Fig. 7. (**A**) The blood vessels of chorioallantoic membrane (CAM) within the ring O in pre- and 10 min post-PTT. The arrow indicates the area of vascular destruction. Scale bar = 20 µm, magnification 10×. The diagrams shown are representative of each group with similar observations. (**B**) The percentage of vascular destruction of all groups at 10 min post-PTT. Data are presented as means ± SEM ($n = 5$), #$p < 0.0001$, saline-treated control vs. QuCy7and QuCy7@mPEG NPs; *$p < 0.01$, QuCy7 vs. QuCy7@mPEG NPs based on one way ANOVA. (**C**) The H&E-stained CAM post-PTT of all groups. BV indicates blood vessels; rp indicates rupture of the blood vessels and the red arrow indicates hyperplasia of ectoderm. Scale bar = 100 µm, magnification 1000x. The diagrams shown are representative of each group with similar observations. (**D**) The thickness of CAM of all groups post-PTT. Data are presented as means ± SEM ($n = 3$), #$p < 0.0001$, saline-treated control vs. QuCy7 and QuCy7@mPEG NPs based on one-way ANOVA.

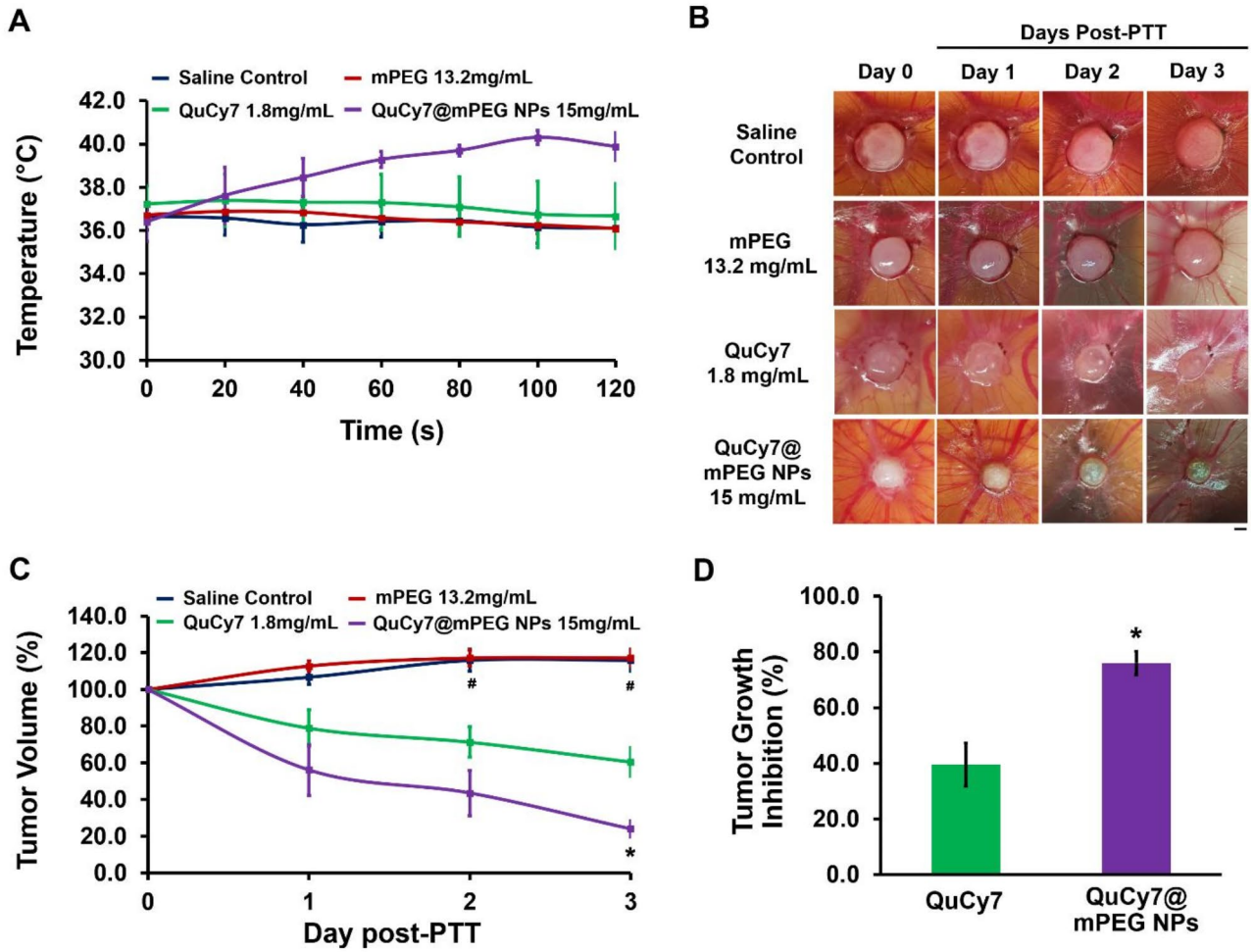

Fig. 8. (**A**). The real-time temperature of the tumor tissues following 120 s of photo-irradiation. Data are presented as means ± SEM ($n = 5$). (**B**) HCT116 cells-derived tumor in CAM pre- (day 0) and post-PTT (days 1, 2, and 3). Scale bar = 20 µm, magnification = 10x. The diagrams shown are representative of each group, same egg for 3 days of observation. (**C**) Percentage of HCT116 tumor volume changes across 3 days of post-PTT. Data are presented as means ± SEM ($n = 5$), #$p < 0.05$, saline-treated control vs. QuCy7 and QuCy7@ mPEG NPs; *$p < 0.05$, QuCy7 vs. QuCy7@mPEG NPs based on one way ANOVA. (**D**) Percentage of *in ovo* HCT116 tumor growth inhibition at day-3 post-PTT. Data are presented as means ± SEM ($n = 5$), *$p < 0.05$, QuCy7 vs. QuCy7@mPEG NPs.

The size of the photo-irradiated tumor tissue in the CAMs in all groups was then measured daily for 72 h. As shown in Fig. 8B and C, there was a minor increase in tumor volume in both saline and mPEG-treated tumors compared to pre-PTT, which indicates no anti-tumor activity. However, the QuCy7 and QuCy7@ mPEG NPs-treated tumors displayed a significant decrease in tumor volume, especially on days 2 and 3. At the equivalent concentration, QuCy7@mPEG NPs demonstrated a better anti-tumor efficacy compared to the QuCy7 at 72 h post-PTT with a reduction in tumor volume by 76.04 ± 4.27% and 39.49 ± 7.80%, respectively ($p = 0.03$) (Fig. 8D). The improvement in the anti-tumor efficacy of QuCy7@mPEG NPs might be attributed to the nanocarrier mPEG, enhancing the delivery and accumulation of QuCy7 in the tumor tissue. This finding is supported by previous studies on the use of heptamethine cyanine as an agent with nanocarriers to improve the delivery and photothermal anti-tumor efficacy[44,45].

Hematoxylin and eosin staining was performed to observe the morphological changes of the tumor tissues post-PTT. In saline and mPEG-treated groups, the tumor tissues were well-vascularized with intact tumor cells. Comparatively, tumoral necrosis was observed in both QuCy7 and QuCy7@mPEG NPs-treated group, with notable hypoplasia (i.e., decrease in cell numbers) and nucleus loss. QuCy7@mPEG NPs-treated group showed necrosis in most of the tumor tissue, compared to QuCy7-treated group (Fig. 9). Major organs were isolated for histopathological analysis on metastasis and PTT-mediated organ toxicity or damage. There were no abnormalities in the morphology of kidney, heart, lung, and liver tissues observed in the chick embryos treated with QuCy7@mPEG NPs (Figure S9). Collectively, these results prove the well-tolerability, good biocompatibility, and potential of QuCy7@mPEG NPs as a promising photothermal agent. This study is the first

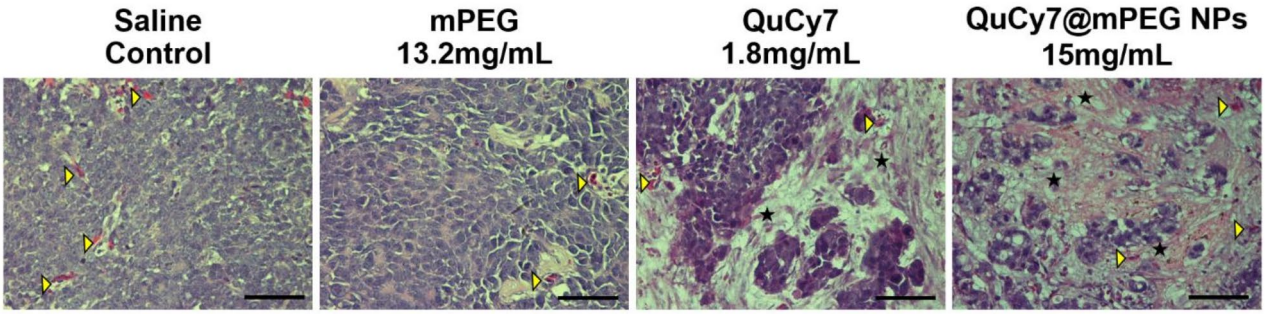

Fig. 9. Hematoxylin and eosin-stained HCT116 cells-derived tumor tissue sections at day 3 post-PTT. The yellow arrowhead indicates blood vessels, and the star indicates the tumor necrotic area (scale bar = 80 μm, magnification = 400×).

to employ the chick embryo model to assess the toxicity and effectiveness of cyanine dye-based nanoparticles in photothermal therapy.

Conclusions

QuCy7, a heptamethine cyanine produced from quinoline, was effectively synthesized with increased water solubility. This dye has outstanding near-infrared absorption beyond 750 nm, as well as remarkable photothermal characteristics. Encapsulating QyCy7 with polyethylene glycol to create nanopolymer QuCy7@mPEG NPs tackles its photoinstability. QuCy7@mPEG NPs have a spherical morphology, with a core-shell structure and a diameter of roughly 120 nm, as detected in TEM. By exposing the NPs to an 808 nm laser for 10 min, the temperature can be increased by up to 24 °C. This is accompanied by a remarkable photothermal conversion (PTC) rate of around 35%. QuCy7@mPEG NPs had better photothermal stability, preserving efficacy after three cycles of radiation exposure as compared to free dye. The *in vitro* PTT studies demonstrate the efficacy of QuCy7@mPEG NPs. Finally, the chick embryo model was employed to assess the nanoparticles' toxicity and efficacy. The results strongly confirm the biocompatibility, photothermal-induced anti-angiogenesis, and anticancer properties of QuCy7@mPEG NPs in the HCT116 xenograft tumor model in the chick embryo.

Experimental section

Synthesis of QuCy7@mPEG NPs

QuCy7 dye was dissolved in DI water. Methoxy polyethylene glycol (mPEG) (Mw = 5000 Da) was added to the solution. The reaction was vigorously stirred at 4 °C for 24 h. NPs were purified by ultrafiltration and washed with cold DI water at least 5 times. The obtained QuCy7@mPEG NPs were resuspended in 10 mL DI water and dried by lyophilization. The concentration of the NPs was calculated from UV − vis-NIR absorbance using a QuCy7 calibration curve (Figure S4). Finally, NPs were stored at -20 °C until use. MALDI-TOF MS ($C_{36}H_{38}ClN_2O_6S_2$-mPEG): calculated $[M+H]^+$: 5694, found: 5328.

Photophysical effect of QuCy7@mPEG NPs

UV − Vis and Fluorescence Measurement. UV visible absorption spectra were obtained from the Cary Series UV-Vis spectrophotometer (Agilent Tech, Santa Clara, CA, USA). The fluorescence spectra were recorded at the excitation wavelengths of 600, 700, 720 750, 780, and 800 nm by the PerkinElmer LS55 fluorescence spectrometer (PerkinElmer, USA) using a quartz cell of 1 cm path length.

The solutions of QuCy7@mPEG NPs in DI water were irradiated with different concentrations under laser 808 nm (1 W/cm^2) for 10 min. The temperature changes were recorded by using a FLIR thermal camera and thermometer digital Nicety DT1311 K-type.

The photothermal conversion efficiency of the **QuCy7@mPEG** was calculated according to the reported method[46,47]:

$$\eta = \frac{hs\,(T_{Max} - T_{Surr}) - Q_{Dis}}{I\,(1 - 10^{-A_{980}})} \tag{1}$$

Where h is the heat transfer coefficient, S is the surface area of the container, and the value of hS is obtained from Eq. 4 and Figure S5B. The maximum steady temperature (T_{max}) of the solution of the **QuCy7@mPEG** was 51.1 °C and environmental temperature (T_{Surr}) was 27 °C. So, the temperature change (T_{Max}-T_{Surr}) of the solution of the **QuCy7@mPEG** was 24.1 °C. The laser power I is 0.525 W. The absorbance of the **QuCy7@mPEG** at 808 nm A_{808} is 0.665. Q_{Dis} expresses heat dissipated from the light absorbed by the solvent and container. The detailed of the calculation was described in ESI.

Cell culture and in vitro assays

Cell culture

The human colorectal carcinoma HCT116 (CCL-274) cell line was purchased from ATCC and cultured in 75 cm^3 culture flasks with Dulbecco's Modified Eagle's Media (DMEM, Hyclone) supplemented with 10% fetal bovine serum (Gibco) and 1% penicillin-streptomycin (Corning). The cells were cultured at 37 °C in a humidified atmosphere containing 5% CO_2.

Cell viability assay

Approximately, 1×10^4 cells/well of HCT116 were seeded into a 96-well cell culture plate for 24 h. Afterward, the cells were incubated with various concentrations of QuCy7@mPEG NPs (0–3 mg/mL) for 24 h. After the incubation, the cells were washed with 0.01 M of PBS pH 7.4 twice before being irradiated with an 808 nm laser (1 W/cm^2) for 5 min and then cultured for another 24 h according to cell culture protocol. 0.5 mg/mL of MTT reagent (Methylthiazolyldiphenyl-tetrazolium bromide, Sigma-Aldrich) in 0.01 M of PBS pH 7.4 solution) was added to the cells and incubated for 2.5 h. Following solution removal, DMSO was added to dissolve the formazan product, which was then detected using a BMG Labtech/SPECTROstar Nano microplate reader capable of UV-vis absorption of formazan at a wavelength of 560 nm. Statistical analysis was performed using Student's t-test ($^*p < 0.05$, $^{**}p < 0.01$, $^{***}p < 0.001$).

LIVE/DEAD assay

Approximately 1×10^4 cells of HCT116 were seeded on 96-well cell culture plates and incubated for 24 h. After that, the cells were incubated with 0, 0.5, and 1.0 mg/mL of QuCy7@mPEG NPs for 24 h. After incubation, the cells were irradiated by an 808 nm laser (1 W/cm^2) for 5 min before further incubation for 24 h. After staining the cells with 4 µM calcein-AM and propidium iodide (Thermo Fisher Scientific) solution in a medium for 5 min, the cells were examined under a fluorescence microscope (BioRad/Zoe) with $\lambda_{ex} = 490$ nm and $\lambda_{em} = 515$ nm for calcein AM and $\lambda_{ex} = 535$ nm and $\lambda_{em} = 615$ nm for PI, respectively.

Chick embryo chorioallantoic membrane (CAM) model

Fertilized chicken eggs of the Lohmann brown variety were purchased from Hing Hong Sdn Bhd, Selangor, Malaysia. The setup of experimental incubation was done following the method as established[48].

Hemocompatibility test of QuCy7@mPEG NPs

The hemocompatibility test was conducted following the procedures with minor modifications[49]. Blood sample was withdrawn from the chick embryo on embryo development day (EDD)-17 using a 27G needle into an ethylenediaminetetraacetic acid (EDTA) tube, followed by centrifugation at 2,000 rpm for 5 min to obtain red blood cells (RBC). The collected RBC was washed with phosphate-buffered saline (PBS) twice. Thereafter, 100 µL of washed RBC was mixed with 100 µL of QuCy7@mPEG NPs at the tested concentrations, followed by incubation at 37 °C for 1 h. Hemoglobin released from the RBC was quantitated following subsequent centrifugation at 2,000 rpm for 5 min by measuring the supernatant spectrophotometrically at 540 nm. The degree of hemolysis (%) was determined using the formula $hemolysis\ (\%) = \frac{Absorbance_{sample} - Absorbance_{blank}}{Absorbance_{positive\ control} - Absorbance_{blank}}$. A blood smear of the RBC was prepared and processed for H&E-stained observation. As controls, RBC was treated with distilled water (positive control) and PBS solution (negative control), respectively.

In ovo acute toxicity of NPs in chick embryos

QuCy7@mPEG NPs and QuCy7 were dissolved and prepared as a stock cocktail in cremophor/ethanol (1:1), while mPEG was dissolved in normal saline. Further dilution was done on the dissolved compounds with injectable normal saline to the desired concentrations to a final volume of 20 µL for administration. On EDD-10, the healthy developing embryos ($n = 5$) were randomly selected and intravenous microinjection (20 µL/embryo) of QuCy7@mPEG NPs was done at three selected concentrations (5, 10 and 15 mg/mL) into the chick embryo using a Hamilton microliter capillary glass syringe with a 33-gauge needle. QuCy7 (1.8 mg/mL; equivalent to the QuCy7 content in QuCy7@mPEG NPs at 15 mg/mL) and mPEG (13.2 mg/mL; equivalent to the mPEG content in QuCy7@mPEG NPs at 15 mg/mL) at 20 µL/embryo were also intravenously administered into the chick embryo. The mortality rate of the chick embryos was monitored at 24 h and 48 h post-administration. Mortality was considered if immobility and cloudy contents were observed.

PTT-induced anti-angiogenesis

The *in ovo* PTT-induced anti-angiogenesis study was conducted following the procedure as established with minor modifications[14]. Briefly, QuCy7@mPEG NPs at the nontoxic concentration (0.3 mg/embryo; 15 mg/mL), with an equivalent dose of mPEG (0.264 mg/embryo; 13.2 mg/mL) and QuCy7 (0.036 mg/embryo; 1.8 mg/mL), was injected intravenously into the chick embryos (EDD-10) at 20 µL/embryo ($n = 5$ per group). A disinfected ring O was gently placed on the CAM for blood vessel spot identification. At 15 min post-administration, photo-irradiation was done with an 808 nm laser at 300 mW/cm^2 at the targeted blood vessels for 120 s. The ring O-marked vasculature of CAMs was photographed under a stereomicroscope (10X) at 10 min post-PTT. Quantification of the targeted blood vessels within the region of ring O was done at pre- and 10 min post-PTT. The chorioallantoic membrane was collected at 10 min post-PTT and processed for histology analysis.

Development of HCT116 Tumor in CAM and *in ovo* PTT

Human HCT116 colorectal carcinoma cell suspension (5×10^5 cells/embryo) in DMEM media was prepared and mixed with growth factor-reduced Matrigel (8.9 mg/mL) at a 1:1 ratio. A disinfected silicon ring O was placed on

the CAM (EDD-10) to enclose a targeted area riched with blood vessels, where 25 µL/embryo of cells-Matrigel mixture was loaded on the CAM within the ring O. Thereafter, the eggs were sealed with parafilm and returned to the incubator. At day 4 post-tumor implantations (EDD-14), the solid tumor grown on CAMs was monitored and randomly grouped for the *in ovo* PTT antitumor study. QuCy7@mPEG NPs, mPEG and QuCy7 (equivalent dose as described above) at 20 µL/embryo were administered intravenously into the chick embryos ($n = 5$ per group). At 15 min post-administration, tumor tissue was irradiated with an 808 nm laser at 300 mW/cm^2 for 120 s. The localized real-time temperature at the irradiated tumor was monitored throughout the 120 s of photo-irradiation by using the Infra-red Thermal Imager. Tumor volume measurement was done using the calipers at 24, 48, and 72 h post-PTT. The tumor volume (mm^3) was calculated following the equation of volume [(tumor width)^2 × tumor length/ 2].

Histopathology analysis

The harvested chorioallantoic membrane, tumor tissues, and organs were processed for histopathology analysis following the procedure as established[43]. On EDD-17, the chick embryo was dissected for the collection of tumor, liver, kidney, heart, and lung tissues and fixed in 10% neutral buffered formalin. The fixed tissues were dehydrated in ascending concentrations of ethanol (70%, 90%, and 100%), followed by clearing in xylene. The cleared tissues were then embedded in paraffin blocks, cut into 5 µm thick sections, and stained with H&E.

Statistical analysis

All data were analyzed and compared using the one-way ANOVA (IBM SPSS version 26). $p < 0.05$ is considered statistically significant.

Data availability

All data generated or analyzed during this study are included in this published article and its supplementary information files.

Received: 14 October 2024; Accepted: 12 December 2024
Published online: 06 January 2025

References

1. Farzam, O. R. et al. Nanoparticles for imaging-guided photothermal therapy of colorectal cancer. *Heliyon* **9**(11), e21334. (2023).
2. Maeda, H., Wu, J., Sawa, T., Matsumura, Y. & Hori, K. Tumor vascular permeability and the EPR effect in macromolecular therapeutics: a review. *J. Control Release* **65**(1-2), 271–284 (2000).
3. Gavas, S., Quazi, S. & Karpinski, T. M. Nanoparticles for Cancer Therapy: Current Progress and Challenges. *Nanoscale Res. Lett.* **16**(1), 173 (2021).
4. Huang, X., El-Sayed, I. H., Qian, W. & El-Sayed, M. A. Cancer cell imaging and photothermal therapy in the near-infrared region by using gold nanorods. *J. Am. Chem. Soc.* **128**(6), 2115–2120 (2006).
5. Wang, R. et al. Surface-Functionalized Modified Copper Sulfide Nanoparticles Enhance Checkpoint Blockade Tumor Immunotherapy by Photothermal Therapy and Antigen Capturing. *ACS Appl. Mater. Interfaces* **11**(15), 13964–13972 (2019).
6. Abed, Z. et al. Iron oxide-gold core-shell nano-theranostic for magnetically targeted photothermal therapy under magnetic resonance imaging guidance. *J. Cancer Res. Clin. Oncol.* **145**(5), 1213–1219 (2019).
7. Parchur, A. K. et al. Vascular Interventional Radiology-Guided Photothermal Therapy of Colorectal Cancer Liver Metastasis with Theranostic Gold Nanorods. *ACS Nano* **12**(7), 6597–6611 (2018).
8. Sun, Y., Chen, H., Liu, G., Ma, L. & Wang, Z. The controllable growth of ultrathin MnO(2) on polydopamine nanospheres as a single nanoplatform for the MRI-guided synergistic therapy of tumors. *J. Mater. Chem. B* **7**(45), 7152–7161 (2019).
9. Cheng, L., Wang, C., Feng, L., Yang, K. & Liu, Z. Functional nanomaterials for phototherapies of cancer. *Chem. Rev.* **114**(21), 10869–10939 (2014).
10. Day, E. S., Morton, J. G. & West, J. L. Nanoparticles for thermal cancer therapy. *J. Biomech. Eng.* **131**(7), 074001 (2009).
11. Estelrich, J. & Busquets, M. A. *Iron Oxide Nanopart. Photothermal Therapy Molecules [Online].* (2018).
12. Feng, W. et al. In vitro and in vivo toxicity studies of copper sulfide nanoplates for potential photothermal applications. *Nanomedicine* **11**(4), 901–912 (2015).
13. Jung, H. S. et al. Organic molecule-based photothermal agents: an expanding photothermal therapy universe. *Chem. Soc. Rev.* **47**(7), 2280–2297 (2018).
14. Chansaenpak, K. et al. Aza-BODIPY-based polymeric nanoparticles for photothermal cancer therapy in a chicken egg tumor model. *Nanoscale Adv.* **6**(2), 406–417 (2024).
15. Li, J. et al. Synthesis, structure and photochemical properties of asymmetric NMe2-bearing aza-BODIPYs as novel photothermal agents. *Dyes Pigm.* **199**, 110092 (2022).
16. Jin, C. S., Lovell, J. F., Chen, J. & Zheng, G. Ablation of hypoxic tumors with dose-equivalent photothermal, but not photodynamic, therapy using a nanostructured porphyrin assembly. *ACS Nano* **7**(3), 2541–2550 (2013).
17. Lovell, J. F. et al. Porphysome nanovesicles generated by porphyrin bilayers for use as multimodal biophotonic contrast agents. *Nat. Mater.* **10**(4), 324–332 (2011).
18. Cai, Y. et al. Correction to Diketopyrrolopyrrole-Triphenylamine Organic Nanoparticles as Multifunctional Reagents for Photoacoustic Imaging-Guided Photodynamic/Photothermal Synergistic Tumor Therapy. *ACS Nano* **17**(11), 11072 (2023).
19. Spence, G. T., Hartland, G. V. & Smith, B. D. Activated photothermal heating using croconaine dyes. *Chem. Sci.* **4**(11), 4240–4244 (2013).
20. Spence, G. T. et al. Near-infrared croconaine rotaxanes and doped nanoparticles for enhanced aqueous photothermal heating. *Chemistry* **20**(39), 12628–12635 (2014).
21. Gao, F. P. et al. Supramolecular adducts of squaraine and protein for noninvasive tumor imaging and photothermal therapy in vivo. *Biomaterials* **35**(3), 1004–1014 (2014).
22. Zheng, X., Xing, D., Zhou, F., Wu, B. & Chen, W. R. Indocyanine green-containing nanostructure as near infrared dual-functional targeting probes for optical imaging and photothermal therapy. *Mol. Pharm.* **8**(2), 447–456 (2011).
23. Pan, W. et al. ICG-Loaded PEG-Modified Black Phosphorus Nanosheets for Fluorescence Imaging-Guided Breast Cancer Therapy. *ACS Omega* **6**(51), 35505–35513 (2021).
24. Feng, L., Chen, W., Ma, X., Liu, S. H. & Yin, J. Near-infrared heptamethine cyanines (Cy7): from structure, property to application. *Org. Biomol. Chem.* **18**(46), 9385–9397 (2020).

25. Leitao, M. M., de Melo-Diogo, D., Alves, C. G., Lima-Sousa, R. & Correia, I. J. Prototypic Heptamethine Cyanine Incorporating Nanomaterials for Cancer Phototheragnostic. *Adv. Healthc. Mater.* **9**(6), e1901665. (2020).
26. Qiu, Y. et al. Recent progress on near-infrared fluorescence heptamethine cyanine dye-based molecules and nanoparticles for tumor imaging and treatment. *Wiley Interdiscip Rev. Nanomed. Nanobiotechnol.* **15**(5), e1910 (2023).
27. Cheng, L. et al. PEGylated Micelle Nanoparticles Encapsulating a Non-Fluorescent Near-Infrared Organic Dye as a Safe and Highly-Effective Photothermal Agent for In Vivo Cancer Therapy. *Adv. Funct. Mater.* **23**(47), 5893–5902 (2013).
28. Yue, C. et al. IR-780 dye loaded tumor targeting theranostic nanoparticles for NIR imaging and photothermal therapy. *Biomaterials* **34**(28), 6853–6861 (2013).
29. Ilina, K. & Henary, M. Cyanine Dyes Containing Quinoline Moieties: History, Synthesis, Optical Properties, and Applications. *Chemistry* **27**(13), 4230–4248 (2021).
30. Diez-Cabanes, V., Monari, A. & Pastore, M. Competition between the Photothermal Effect and Emission in Potential Phototherapy Agents. *J. Phys. Chem. B* **125**(31), 8733–8741 (2021).
31. Bahmani, B. et al. Effects of nanoencapsulation and PEGylation on biodistribution of indocyanine green in healthy mice: quantitative fluorescence imaging and analysis of organs. *Int. J. Nanomed.* **8**, 1609–1620 (2013).
32. Peters, M. et al. PEGylating poly(p-phenylene vinylene)-based bioimaging nanoprobes. *J. Colloid Interface Sci.* **581**, 566–575 (2021).
33. Soroushian, B. & Yang, X. Measuring non-radiative relaxation time of fluorophores with biomedical applications by intensity-modulated laser-induced photoacoustic effect. *Biomed. Opt. Express* **2**(10), 2749–2760 (2011).
34. Al-Rawashdeh, N. Current Achievement and Future Potential of Fluorescence Spectroscopy. (2012).
35. Setyawati, M., Tay, C. Y., Docter, D., Stauber, R. & Leong, D. *Understanding and Exploiting Nanoparticles' Intimacy with the Blood Vessel and Blood. CHEM SOC REV 2015* (Chemical Society Reviews, 2015).
36. Ye, M., Gong, J., Chen, W., Liu, X. & Zhu, D. Effect of the size of nucleic acid delivery systems on their fate in cancer treatment. *Explor. Drug Sci.* **2**(1), 38–49 (2024).
37. Subhan, M. A., Parveen, F., Filipczak, N., Yalamarty, S. S. & Torchilin, V. P. Approaches to Improve EPR-Based Drug Delivery for Cancer Therapy and Diagnosis. *J. Personalized Med. [Online]*. (2023).
38. Anders, C. B., Chess, J. J., Wingett, D. G. & Punnoose, A. Serum Proteins Enhance Dispersion Stability and Influence the Cytotoxicity and Dosimetry of ZnO Nanoparticles in Suspension and Adherent Cancer Cell Models. *Nanoscale Res. Lett.* **10**(1), 448 (2015).
39. Smith, M. C., Crist, R. M., Clogston, J. D. & McNeil, S. E. Zeta potential: a case study of cationic, anionic, and neutral liposomes. *Anal. Bioanal. Chem.* **409**(24), 5779–5787 (2017).
40. Doane, T. L., Chuang, C. H., Hill, R. J. & Burda, C. Nanoparticle ζ -Potentials. *Acc. Chem. Res.* **45**(3), 317–326 (2012).
41. Butler, K. S., Brinker, C. J. & Leong, H. S. Bridging the In Vitro to In Vivo gap: Using the Chick Embryo Model to Accelerate Nanoparticle Validation and Qualification for In Vivo studies. *ACS Nano* **16**(12), 19626–19650 (2022).
42. de Alves, C. S. et al. Chicken embryo model for in vivo acute toxicological and antitumor efficacy evaluation of lipid nanocarrier containing doxorubicin. *Int. J. Pharm. X* **6**, 100193 (2023).
43. Kampaengsri, S. et al. PEGylated Aza-BODIPY Nanoparticles for Photothermal Therapy. *ACS Appl. Bio Mater.* (2022).
44. Lin, W. et al. Near-Infrared Polymeric Nanoparticles with High Content of Cyanine for Bimodal Imaging and Photothermal Therapy. *ACS Appl. Mater. Interfaces* **8**(37), 24426–24432 (2016).
45. Pan, G. Y., Jia, H. R., Zhu, Y. X. & Wu, F. G. Turning double hydrophilic into amphiphilic: IR825-conjugated polymeric nanomicelles for near-infrared fluorescence imaging-guided photothermal cancer therapy. *Nanoscale* **10**(4), 2115–2127 (2018).
46. Li, C. Q. et al. In situ synthesis of multifunctional tellurium nanorods stabilized by polypeptide-engineered for photothermal-sonodynamic combination therapy of tumors. *Chem. Eng. J.* **417**, 127989 (2021).
47. Saiyasombat, W. et al. NIR-induced antimicrobial efficacy of TPA-BOIMPY conjugate through photothermal and photodynamic synergy. *J. Photochem. Photobiol., A* **460**, 116136 (2025).
48. Kue, C. S., Tan, K. Y., Lam, M. L. & Lee, H. B. Chick embryo chorioallantoic membrane (CAM): an alternative predictive model in acute toxicological studies for anti-cancer drugs. *Exp. Anim.* **64**(2), 129–138 (2015).
49. Kutwin, M. et al. Structural damage of chicken red blood cells exposed to platinum nanoparticles and cisplatin. *Nanoscale Res. Lett.* **9**(1), 257 (2014).

Acknowledgements

This work received funding support from the NSRF via the Program Management Unit for Human Resources & Institutional Development, Research and Innovation [grant number B38G670011]; Management & Science University Seed Research Grant (SG-026-012023-FHLS), and by (i) Suranaree University of Technology (SUT), (ii) Thailand Science Research and Innovation (TSRI), (iii) National Science, Research and Innovation Fund (NSRF), NRIIS number 204274.

Author contributions

S.A. and S.K. synthesized and characterized a compound. T.P. and B.O. conceived all the cell assays. G Y. Y. performed all *in ovo* experiments. K.C., S.J., C-S. K., and A.K. validated the results. S.K., S.A., G Y. Y., C-S. K. and A.K. wrote the first draft manuscript. All authors reviewed the manuscript.

Declarations

Competing interests

The authors declare no competing interests.

Additional information

Supplementary Information The online version contains supplementary material available at https://doi.org/10.1038/s41598-024-83249-y.

Correspondence and requests for materials should be addressed to C.-S.K. or A.K.